Morphology controllable urchin-shaped bimetallic nickel-cobalt oxide/carbon composites with enhanced electromagnetic wave absorption performance

Fushan Li[a], Qiuyu Li[a], Hideo Kimura[a], Xiubo Xie[a], Xiaoyu Zhang[a,b], Nannan Wu[c], Xueqin Sun[a], Ben Bin Xu,[e] Hassan Algadi[h,d], Rami Adel Pashameah,[i] Abdullah K. Alanazi[j], Eman Alzahrani[j], Haodong Li[f], Wei Du[a]*, Zhanhu Guo[f,g]*, Chuanxin Hou[a]*

a. School of Environmental and Material Engineering, Yantai University, Yantai, 264005, China
b. Shandong Laboratory of Yantai Advanced Materials and Green Manufacturing, Yantai, 264005, China
c. School of Material Science and Engineering, Shandong University of Science and Technology, Qingdao, 266590, China
d. College of Materials Science and Engineering, Taiyuan University of Science and Technology, Taiyuan, 030024, China
e. Mechanical and Construction Engineering, Faculty of Engineering and Environment, Northumbria University, Newcastle Upon Tyne, NE1 8ST, UK
f. Integrated Composites Laboratory (ICL), Mechanical and Construction Engineering, Northumbria University, Newcastle Upon Tyne, NE1 8ST, UK
g. Department of Chemical and Bimolecular Engineering, University of Tennessee, Knoxville, TN, 37996, United States
h. Department of Electrical Engineering, Faculty of Engineering, Najran University, Najran, 11001, Saudi Arabia
i. Department of Chemistry, Faculty of Applied Science, Umm Al-Qura University, Makkah 24230, Saudi Arabia
j. Department of Chemistry, College of Science, Taif University, P.O. Box 11099, Taif 21944, Saudi Arabia

Corresponding Authors:

Wei Du: duwei@ytu.edu.cn; Zhanhu Guo: zhanhu.guo@northumbria.ac.uk

Chuanxin Hou: chuanxin210@ytu.edu.cn

Abstract

The microscopic morphology of electromagnetic wave absorbers influences the multiple reflections of electromagnetic waves and impedance matching, determining the absorption properties. Herein, the urchin-shaped bimetallic nickel-cobalt oxide/carbon ($NiCo_2O_4$/C) composites are prepared via a hydrothermal route, whose absorption properties are investigated by different morphologies regulated by changing calcination temperature. A minimum reflection loss (RL_{min}) of -75.26 dB is achieved at a matching thickness of 1.5 mm, and the effective absorption bandwidth (EAB) of 8.96 GHz is achieved at 2 mm. Multi-advantages of the synthesized $NiCo_2O_4$/C composites contribute to satisfactory absorption properties. First, the interweaving of the needle-like structures increases the opportunities for scattering and multiple reflections of incident electromagnetic waves, and builds up a conductive network to facilitate the enhancement of conductive losses. Second, the carbon component in the $NiCo_2O_4$/C composites enhances the interfacial polarization and reduces the density of the absorber. Besides, generous oxygen vacancy defects are introduced into the $NiCo_2O_4$/C composites, which induces defect polarization and dipole polarization. In summary, the ternary coordination of components, defects and morphology led to outstanding electromagnetic wave absorption, which lightened the path for improving the electromagnetic wave absorption property and enriching the family of $NiCo_2O_4$ absorbers with excellent performance.

Keywords: $NiCo_2O_4$/C; Oxygen vacancies; Interfacial polarization; Electromagnetic wave absorber.

1. Introduction

In modern society, more and more wireless electronic devices rely on electromagnetic waves to transmit information, which brings convenience to our lives [1-11]. However, serious electromagnetic pollution is silently produced, and affects the health of humans and other organisms. Meanwhile, electromagnetic (EM) wave that is emitted during the operation of precision instruments applied in the scientific or medical industry affects their regular operation and maintenance. Nowadays, the EM waves generated by the equipment can be exhausted via EM wave absorbers and converted to other energy forms to realize the consumption of EM waves. In addition to the civil field, EM wave-absorbing materials are also applied in the military field. For example, coatings containing wave-absorbing materials can effectively improve the concealment ability of fighter planes and warships, which has far-reaching significance in enhancing national defense strength. To achieve the high-efficient EM wave absorbers with the characteristics of absorbent, lightweight, thin, and broadband, multitudinous materials, including carbon-based materials, ferrite, metals and alloys, conductive polymers, ceramics, et al. were explored [12-22].

Bimetallic nickel-cobalt oxide is a typical ferrite material with a spinel structure, where cobalt ions occupy the tetrahedral and octahedral location while nickel ions occupy the octahedral position [23, 24]. It inherits the superiorities of ferrite, including low synthetic cost, controllable morphology, and high polarization capacity, promoting to be the potential material capable of achieving superb EM wave absorption performance. Numerous bimetallic nickel-cobalt oxides with different micro/nano morphologies, including nanoparticles, nanorods, nanosheets,

nanoflowers, porous hollow spheres, core-shell structures, three-dimensional framework structures, etc., have been investigated as EM wave absorbers. For instance, a layered self-assembled $NiCo_2O_4$ nanoflower structure was obtained, whose microwave absorption performance was evaluated with an minimum reflection loss (RL_{min}) of -45.5 dB and an the effective absorption bandwidth (EAB) of 7.7 GHz at a matched thickness of 4.2 mm. The satisfactory performance was owing to the strong dielectric loss capability of the $NiCo_2O_4$ and the superimposed lamellar structure, which enhances the conductive losses and the reflection and scattering of incident EM waves [25]. Meanwhile, a three-dimensional framework structure consisting of short conical $NiCo_2O_4$ and wood-derived carbon was achieved and yieleded outstanding absorption properties (an EAB of 8.08 GHz at 3.62 mm). The interfacial and dipole polarization induced by interfaces and defects in the composites enhanced the EM wave absorption properties and addressed the high density of $NiCo_2O_4$ with the introduction of wood-derived carbon [26].

Although satisfactory EM wave absorption performance of $NiCo_2O_4$-based absorbers has gained, the issue of large matching thicknesses still hinders its further application. The $NiCo_2O_4$-based absorbers with hollow spherical and nano-rod structures can achieve an EAB value close to the above-mentioned morphological orientation at a small matching thickness. The hollowed structure facilitates optimal impedance matching, increases the amount of incident EM waves, and allows for multiple scattering and reflections of EM waves within the cavity [27, 28]. For example, multilayer hollow sphere-shaped $NiCo_2O_4$ materials were prepared and exhibited an EAB of 5.92 GHz at 2.14 mm [27]. The nano-rod-like structures are interwoven to build a

complex conductive network, which increases the electron transport pathway in favor of enhancing conductive losses, leading to energy consumption when micro-currents were generated in the EM field. The nano-rod structures were always constructed to act as EM wave absorbers. The $NiCo_2O_4$ with rod-like structure was prepared and presented an EAB of 6.08 GHz at 1.88 mm [29]. Furthermore, the urchin-like structure, combining the advantages of a hollow sphere and a needle-like structure, was believed to be an ideal EM wave absorber structure, which allows the incident EM waves multiply reflected and scattered between the needle-like and hollow spherical structures, resulting in the effective energy attenuation of the EM waves. Therefore, the conductive network formed by an urchin-like structure presents colossal potential for excellent wave absorption properties due to the increased transmission pathways for electrons and enhanced conductive losses [30-34]. Some researchers have focused on $NiCo_2O_4$ absorbers with urchin-like structures, for example, the hollow urchin-like structure achieved satisfactory effective absorption bandwidths at low matching thicknesses, with an EAB of 5.81 GHz [34]. Nevertheless, the effective absorption bandwidth of $NiCo_2O_4$-based absorbers still needs to be broadened.

Herein, the bimetallic nickel-cobalt oxide/carbon composites ($NiCo_2O_4$/C) with the uniquely designed hollow urchin-like structures are achieved via a facile hydrothermal method accompanying with a heat treatment process. The magnetic properties, morphologies and components of $NiCo_2O_4$/C composites are explored by varying the calcination temperature. The distinctive urchin-like structure, and the introduction of carbon and oxygen vacancy defects enable all the prepared samples to exhibit outstanding EM wave absorption behaviors. The

optimized composites presented a broadened EAB of 8.96 GHz at 2.0 mm and an RL_{min} of -75.26 dB at 1.5 mm. Synergistic effects of morphology, elements and oxygen vacancy defects regulation in this work will shed light on the optimization and utilization of bimetallic nickel-cobalt oxides as EM wave absorbers, and offer originalities on improving broadened absorption bandwidth of bimetallic nickel-cobalt oxides or other absorbers.

2. Results and discussion

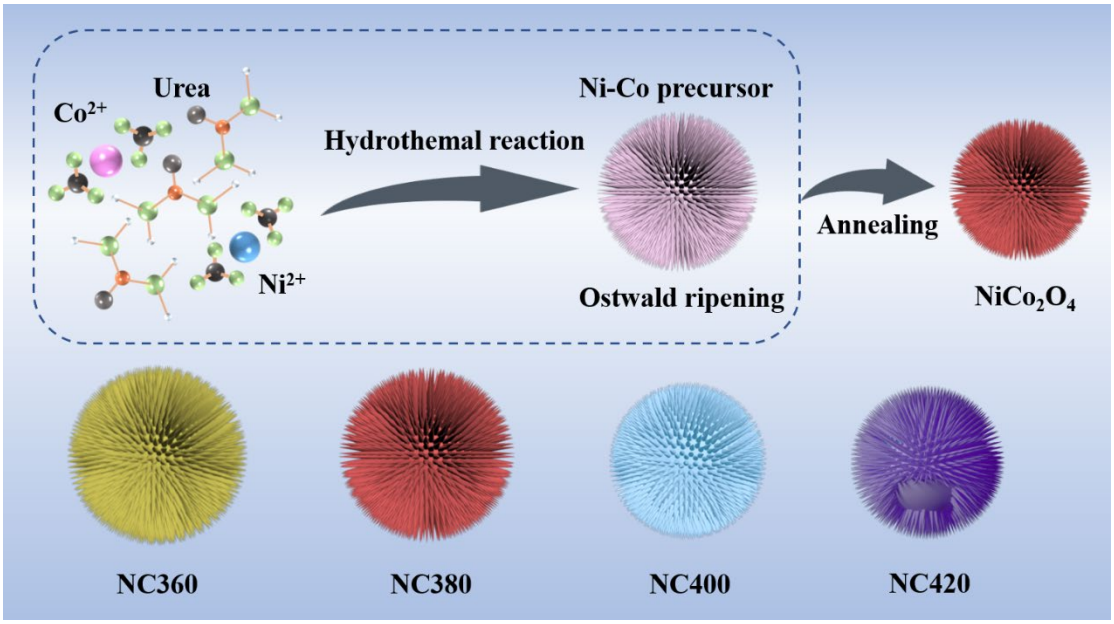

Scheme 1 Mechanism diagram for the synthesis of urchin-like $NiCo_2O_4$/C hybrids.

The synthetic route of preparing urchin-like $NiCo_2O_4$/C composites with hollow microspheres and oxygen vacancy defects is displayed in **Scheme 1**, and the formation mechanism is illustrated by Eqns. 1-6:

$$CO(NH_2)_2 + H_2O \rightarrow 2NH_3 + CO_2 \quad (1)$$

$$NH_3 + H_2O \rightarrow NH^{4+} + OH^- \quad (2)$$

$$CO_2 + H_2O \rightarrow CO_3^{2-} + 2H^+ \quad (3)$$

$$2Ni^{2+} + 2OH^- + CO_3^{2-} \rightarrow Ni_2(CO_3)(OH)_2 \quad (4)$$

$$2Co^{2+} + 2OH^- + CO_3^{2-} \rightarrow 2Co(CO_3)_{0.5}(OH) \quad (5)$$

$$Ni_2(CO_3)(OH)_2 + 4Co(CO_3)_{0.5}(OH) + O_2 \rightarrow 2NiCo_2O_4 + 3CO_2 + 3H_2O \quad (6)$$

First, the CO_3^{2-} and OH^- in the solution offered by the decomposition of urea during the hydrothermal process combined with Ni^{2+} and Co^{2+} to form a complex compound. Then, the hollow microsphere precursor was formed from the complex compound according to Ostwald ripening mechanism [35]. The final $NiCo_2O_4$/C composites were obtained after a simple heat treatment process under air atmosphere at different temperatures. The oxygen vacancy defects are generated due to the reaction between residual carbon in the complex compound and oxygen atoms in $NiCo_2O_4$, which is speculated to improve the wave absorption abilities of the composites. The composites obtained at different temperatures (such as 360 °C, 380 °C, 400 °C and 420 °C) were marked as NC360, NC380, NC400 and NC420, respectively, the detailed information is presented in experimental section (Supporting information).

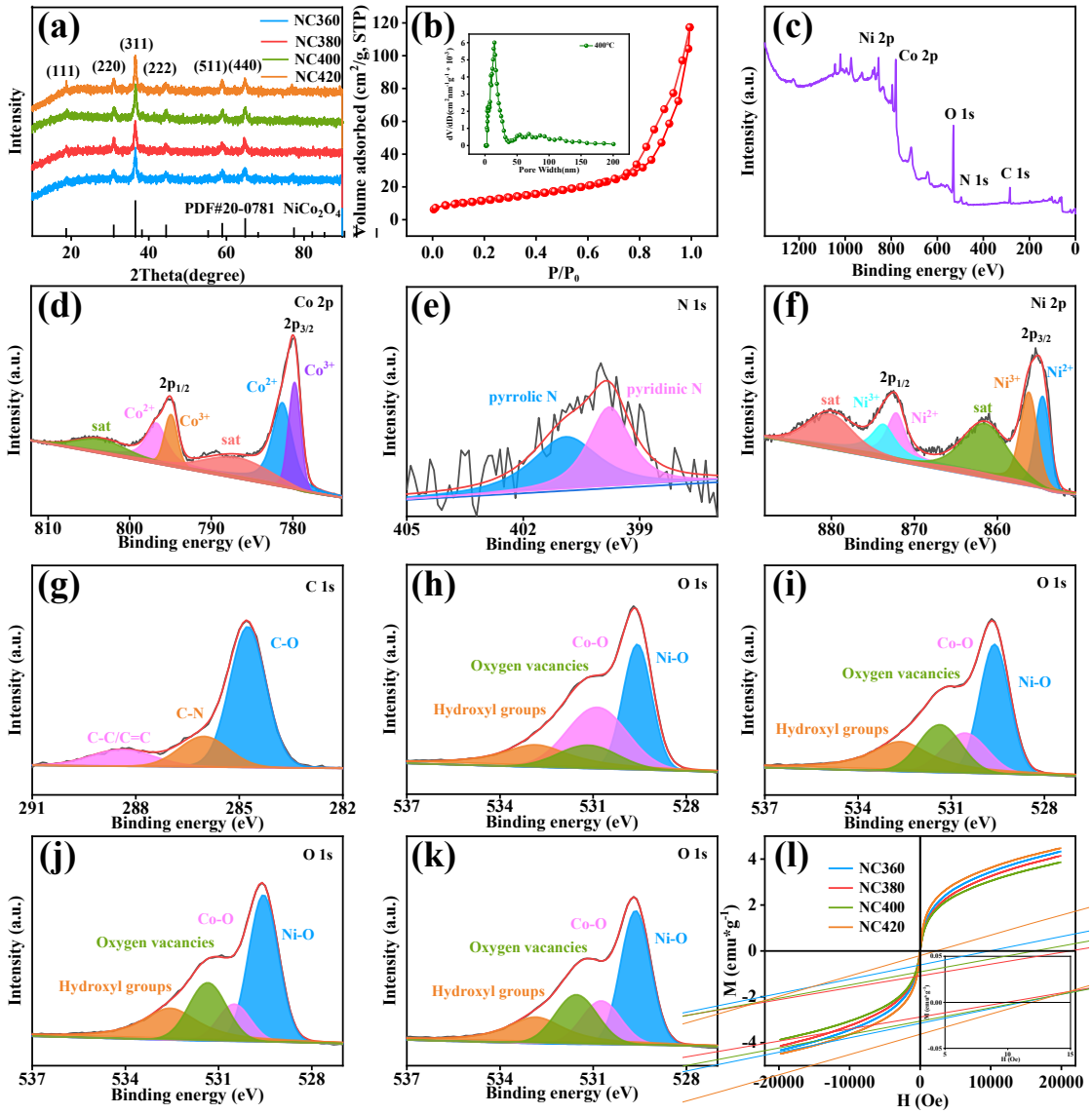

Fig. 1 a) The XRD patterns, b) the nitrogen adsorption-desorption isotherms and the pore size distribution, c) XPS survey spectra, high-resolution XPS spectra of d) Co 2p, e) N 1s, f) Ni 2p, g) C 1s of NC380 composites and h-k) O 1s and l) magnetic properties of all composites.

The X-ray diffraction (XRD) patterns are captured to offer the crystal information of the prepared precursors and $NiCo_2O_4$/C composites, which are shown in **Fig. S1** and **Fig.1**a. The precursors are identified as the composites of $Co(CO_3)_{0.5}(OH)\cdot 0.11H_2O$ and $Ni_2(CO_3)(OH)_2$ due to the peaks accord to the JCPDS: 48-0083 and JCPDS: 35-0501, respectively [36]. The

composition and phase information of the final obtained composites are collected by XRD test in Fig.1a. The distinctive primary peaks located at 18.9, 31.1, 36.7, 38.4, 59.0 and 64.9° are distinguished to the (111), (220), (311), (222), (511), and (440) planes of cubic spinel $NiCo_2O_4$ (PDF#20-0781) [16], which proves the successful synthesis of $NiCo_2O_4$.

N_2 adsorption/desorption isotherm and pore size distribution of NC380 composites are monitored and the result is shown in Fig. 1b. The isotherm illustrates the mesoporous structure of the $NiCo_2O_4$ composites [37-39]. The Brunauer-Emmett- Teller (BET) specific surface area of NC380 is calculated to be *ca*. 43.1 $m^2\ g^{-1}$, and its pore size distribution is concentered within 2-40 nm. The results prove the formation of mesoporous structures, which will facilitate the injection of EM waves and multiple reflections within it, and the large BET value will reduce the density of absorbers, promoting their practical application with the characteristic of lightness.

To probe the chemical composition and valence state information of the $NiCo_2O_4$ composites, the X-ray photoelectron spectrometer (XPS) measurement is applied and shown in Fig. 1d-k. The predominant peaks in Fig. 1d testify the occurrence of C 1s, Ni 2p, Co 2p, N 1s and O 1s in the composites [40]. The high-resolution XPS spectra of Co 2p in Fig. 1d consist of two spin-orbit doublets characteristics of Co^{2+} and Co^{3+}, and two satellite peaks (788 and 804.5 eV). Furthermore, obvious peaks at 780.98 and 796.48 eV are attributed to Co^{2+}, while 794.78 and 779.68 eV are owing to Co^{3+} [41]. Similarly, high-resolution XPS spectra of Ni 2p (Fig.1f) are composed of two satellite peaks (861.7eV and 880.4eV) and to two spin-orbit doublets features of Ni^{2+} and Ni^{3+}. Characteristic peaks at 853.98 and 871.58 eV are attributed to Ni^{2+}, and 855.48 and 873.48 eV are contributed to Ni^{3+} [42]. The N 1s spectra consist of two peaks at 392.1 and 399.8 eV, which are identified to pyridine nitrogen and pyrrole nitrogen, respectively (Fig.1e) [37,39,41]. Meanwhile, the C 1s spectra are composed of three peaks, which are distinguished to

C-O (284.8 eV), C-N (286 eV) and C=C/C-C (288.4 eV), respectively (Fig.1g) [44]. The high-resolution spectra of O 1s are detected to four categories of oxygen species, including Ni-O bond, the Co-O bond, oxygen vacancy and OH^- groups that locate at 529.6, 530.6, 531.4 and 532.7 eV, respectively (Fig. 1h-k) [45]. The XPS results identify the successful preparation of $NiCo_2O_4$/C composites.

Furthermore, the oxygen vacancy defects have been proven to be an important factor for EM wave absorption behaviors [34]. The ratios of the integral area of the oxygen vacancy peaks in Fig. 1h-k are applied to evaluate the relative content of oxygen vacancies (**Table S1**), which proves the existence of oxygen vacancy defects, and the relative concentration of oxygen vacancy can be optimized via heat treatment temperature. The EM wave absorption properties will be improved due to the emergence of oxygen vacancy defects that lead to an uneven charge distribution, thus creating dipole polarization in alternating EM fields and the dissipation of EW waves. The XPS tests of the other $NiCo_2O_4$/C present similar results, which are displayed in **Fig. S2**.

The static magnetic property of $NiCo_2O_4$/C hybrids is presented in Fig. 1l. The saturation magnetization (Ms) values of 4.33, 4.14, 3.86, 4.48 emu g^{-1} are obtained for NC360, NC380, NC400 and NC420, respectively. All the prepared composites show the typical S-shaped hysteresis loops, indicating the ferromagnetic property, and the relatively poor Ms values illustrate the small magnetic loss capacity [46]. Meanwhile, the coercivity values of the composites are all around 12 Oe. The Ms and coercivity for all $NiCo_2O_4$/C composites exhibit similar values due to the slight difference in the anisotropy of the stray flux line density generated by the surface needle-like structure, and shape anisotropy [47].

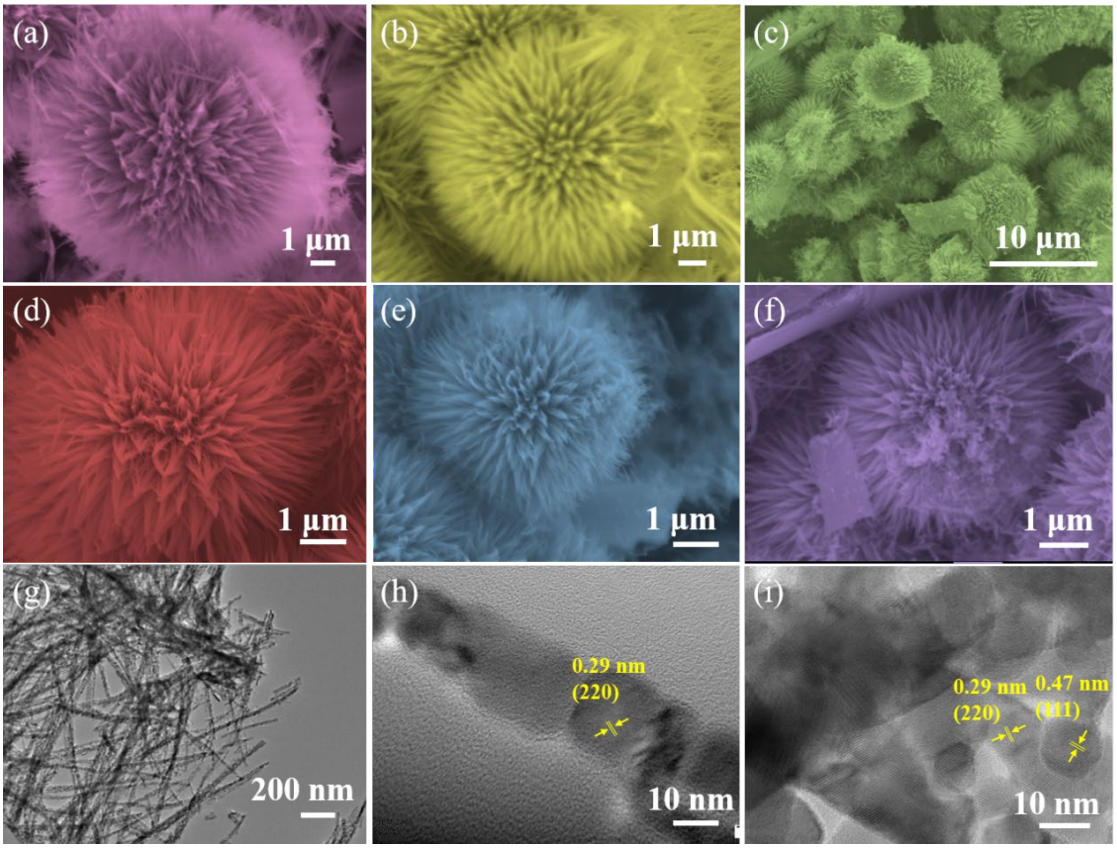

Fig. 2 SEM images of (a) Ni-Co precursor; (b) NC360; (c, d) NC380; (e) NC400 and (f) NC420; TEM images of (g-i) NC380.

The morphologies of Ni-Co precursor and $NiCo_2O_4$/C hybrids are measured utilizing SEM and TEM tests, which are presented in **Fig. 2**. Ni-Co precursor shown in Fig. 2a exhibits the urchin-like structure formed via a self-assemble route with an average diameter ca. 6 μm. Meanwhile, the hollow structure of the Ni-Co precursor stems from the Ostwald ripening mechanism during the hydrothermal process. The final $NiCo_2O_4$/C composites inherit the morphologies of Ni-Co precursor, and their diameter gradually decreases with the increase of calcination temperature (Fig. 2b-2f). The needle-like structure is gradually destroyed and exbibit some bare hollow spherical surface when the temperature is beyond 400 ºC. To further explore the morphologies and composition features of $NiCo_2O_4$ composite, the TEM images of NC380 are displayed in Fig. 2g-i, where the needle-like structures on the surface of NC380 are observed.

The intricate conductive network formed by needle-like structures will enhance the electrical conductivity and optimize the dielectric loss properties of the $NiCo_2O_4$/C composites when applied as absorbers. The lattice spacings of 0.29 and 0.47 nm in Fig. 2h-i are indexed to be the (220) and (111) plane of $NiCo_2O_4$ [47], which illustrates the successful preparation of $NiCo_2O_4$/C associated with XRD and XPS results.

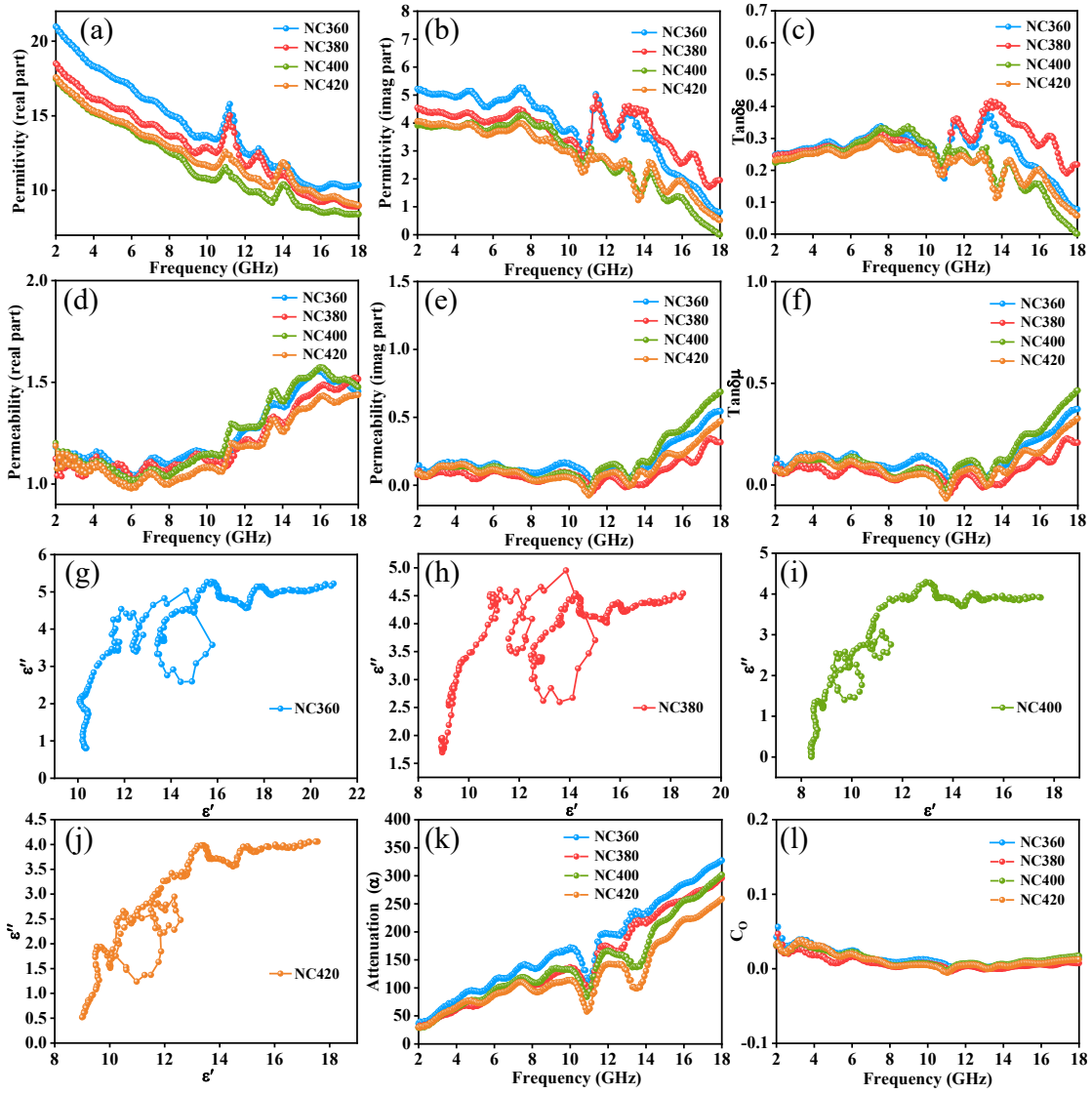

Fig. 3 EM parameters of $NiCo_2O_4$/C composites: (a) real and (b) imaginary part of permittivity; (c) dielectric loss tanδε; (d) real and (e) imaginary part of permeability; (f) magnetic loss tanδμ; (g-j) Cole-Cole semicircles; (k) attenuation constant; and (l) C_0 of samples.

Complex permittivity and permeability are dominant parameters that reflect the wave absorption properties of absorbers, the EM parameters of $NiCo_2O_4$/C composite absorbers are measured and exhibited in **Fig. 3**. The real part (ε') of permittivity for all the absorbers (Fig. 3a) exhibits the similar tendency that decreases gradually with the increasing frequency and accompanied by some fluctuations. The dispersion phenomenon would be caused by the mismatch between the speed of dipole rotation and the change of the high-frequency electromagnetic field. The variation of the dielectric constant is related to the content of carbon, and the degree of graphitization. Initial descent trend of dielectric constant with the temperature increases due to the gradually oxidizes and overflows of carbon matrix, and then increased because of the higher graphitization. The distinguishable resonance peaks in the imaginary part (ε'') of permittivity (Fig. 3b) indicate the presence of multiple Debye relaxation processes. The results are evident that NC360 and NC380 absorbers present a higher value of ε'', which may be attributed to the increased electrical conductivity by the higher degree of shape retention at lower heat treatment temperature, and the higher density of spines on the surface of the spheres [48]. The result also confirms that the dielectric loss capacity property can be tuned by modulating the morphologies of absorbers by temperature. The NC380 sample exhibits higher tangential values of dielectric loss during the 14 to 18 GHz (Fig. 3c), illustrating the better dielectric loss capacity property. In the current generally accepted theory, dielectric losses consist of interfacial polarization, dipole polarization and conductive losses [49]. The prepared $NiCo_2O_4$/C composite presents strong interfacial polarization owing to the composites of $NiCo_2O_4$ and carbon, which form abundant heterogeneous interfaces. Meanwhile, abundant oxygen vacancies produced in the synthesized

composites due to the various heat treatment temperatures act as dipoles in an alternating EM field, inducing the generation of orientational polarization. The mentioned dielectric loss mechanisms can be derived by observing the Cole-Cole semicircle diagram (Fig.3g-j), which can be explained by Debye relaxation theory, relative complex permittivity ε_r is described by Eqn. 7 [40]:

$$\left(\varepsilon' - \frac{\varepsilon_s+\varepsilon_\infty}{2}\right)^2 + (\varepsilon'')^2 = \left(\frac{\varepsilon_0-\varepsilon_\infty}{2}\right)^2 \quad (7)$$

where ε_s means fixed constant, and ε_∞ is dielectric constant. The Cole-Cole semicircle is defined by the semicircles obtained based on Eqn. 7. Multiple semicircles are observed in the plots, indicating the presence of the Debye relaxation process. It is worth noting that the absorber semicircle is distorted, implying the presence of other polarization processes. The tail of the Cole-Cole semicircles indicates the presence of conductive losses, which may originate from the carbon in the absorber [50]. The real part of complex permeability for the $NiCo_2O_4$/C absorbers in Fig. 3d shows a similar tendency that the value keeps almost constant between 2 to 10 GHz and gradually increases after 14 GHz. The obvious resonance peaks in the imaginary part of the magnetic permeability are captured at two regions of 4 to 8 GHz and 10 to 16 GHz, respectively (Fig. 3e), which are in connection with the magnetic loss of the absorbers [51], indicating a high magnetic loss capability of the NC360 and NC400 absorbers numerically. It's accepted that the imaginary part of complex permeability (μ'') is related to magnetic loss. Usually, μ'' is positive. However, negative μ'' will be generated due to the motion of charges under an EM field, which leads to an ac electric field, and then, induces a magnetic field. When the induced magnetic field exceeds the original magnetic field, and releases some magnetic energy in turn, negative value

appears [52,53]. The conclusion is also obtained from magnetic loss tangent value (Fig. 3f). The contribution of eddy current losses of EM wave absorbing materials can generally be expressed by C_0, as Eqn.8 [54]:

$$C_0 = \mu''\mu'^{-1}f^{-2} \quad (8)$$

where f presents the frequency of the incident microwaves, $\mu'$and μ'' means the real and imaginary part of permeability, respectively. The mechanisms of magnetic loss in wave absorbers during 2-18 GHz are believed to be consisted of eddy current loss, exchange resonance and natural resonance. The eddy current loss dominates the magnetic loss if C_0 is a constant in the whole frequency. Therefore, other magnetic loss mechanisms of natural or/and exchange resonances are presented for $NiCo_2O_4$/C absorbers due to the fluctuation of C_0 value in Fig. 3l.

In order to be an excellent EM wave absorber, outstanding attenuation ability needs to be possessed. Attenuation constant (α) is usually applied to evaluate microwave dissipation capability, which is calculated by Eqn. 9 as follows [55]:

$$\alpha = \frac{\pi f\sqrt{2}}{c} \times \sqrt{\mu''\varepsilon'' - \mu'\varepsilon' + \sqrt{(\mu'\varepsilon'' + \mu''\varepsilon')^2 + (\mu''\varepsilon'' - \mu'\varepsilon')^2}} \quad (9)$$

in which c means the speed of the microwave. The α-value of $NiCo_2O_4$/C absorbers in Fig. 3k illustrates that the α-value decreases with the increase of calcination temperature. The analysis of attenuation constant corresponds to the EM wave absorber performance from another angle. Good cooperative effect of attenuation constants and impedance matching is needed to obtain satisfactory effective EM waves absorption behaviors [38]. Consequently, although NC360 composites exbibit a high attenuation capability, it presents relatively poor absorption capability due to poor impedance matching.

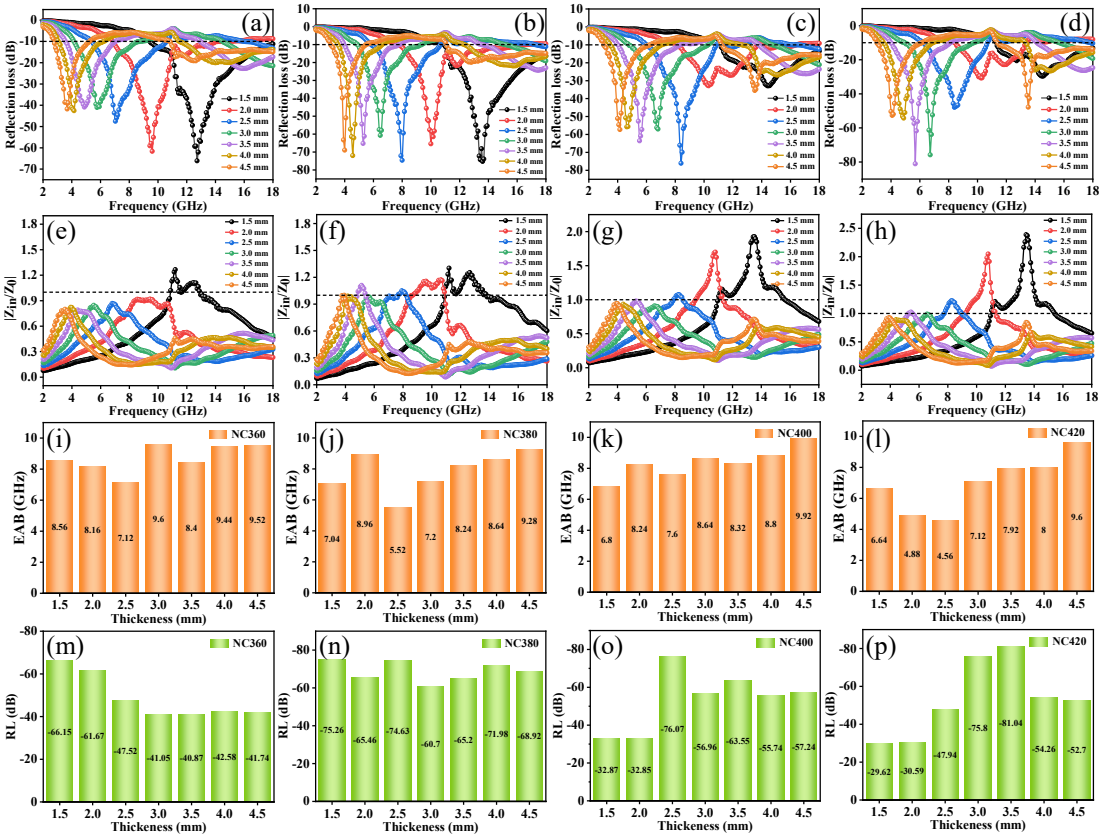

Fig. 4 2D Reflection loss and impedance matching characteristic at different matching thicknesses of (a, e) NC360; (b, f) NC380; (c, g) NC400 and (d, h) NC420. Comparison of (i-l) EAB and (m-p) RL values of $NiCo_2O_4$/C absorbers.

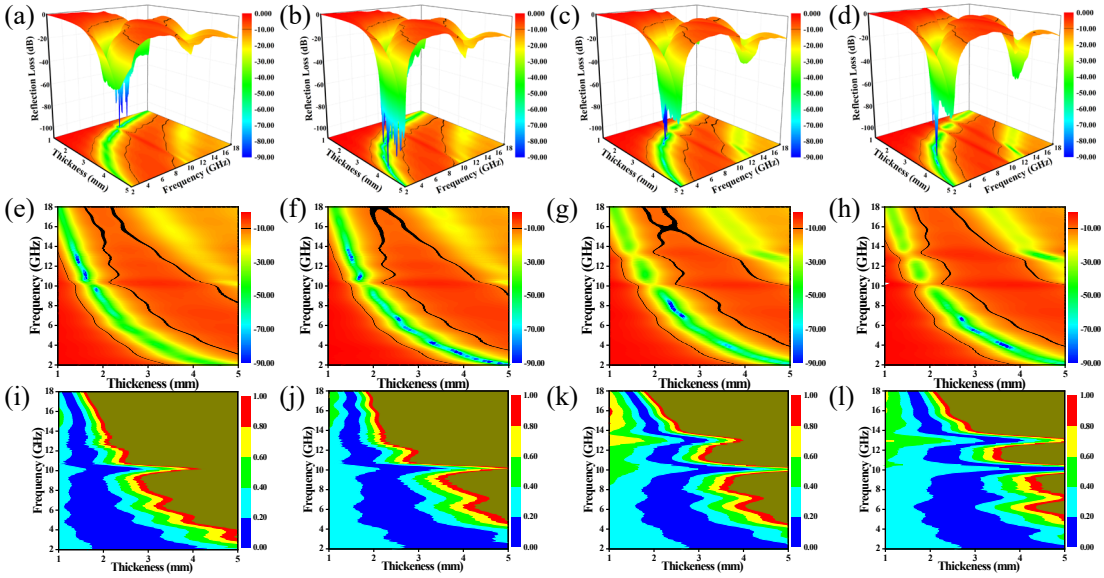

Fig. 5 3D representations, 2D projection images of the calculated RL and calculated delta value

maps of (a, e, i) NC360; (b, f, j) NC380; (c, g, k) NC400 and (d, h, l) NC420.

The reflection loss (RL) values are achieved via EM parameters based on transmission line theory obtained by Eqns.10 and 11 in view of the metal back-panel model [55]:

$$Z_{in} = Z_0\sqrt{\frac{\mu_r}{\varepsilon_r}}\tan h\left|j\left(\frac{2\pi fd}{c}\right)\sqrt{\mu_r\varepsilon_r}\right| \quad (10)$$

$$RL = 20lg\left|\frac{Z_0 - Z_{in}}{Z_0 + Z_{in}}\right| \quad (11)$$

where Z_{in} represents the input impedance of absorbers, Z_0 represents the impedance of free space, μ_r and ε_r represent the complex permittivity ($\varepsilon_r = \varepsilon' - j\varepsilon''$) and the complex permeability ($\mu_r = \mu' - j\mu''$), respectively, f illustrates the frequency of the incident microwaves, d is the thickness of the absorber. Generally, microwave absorption efficiency reaches 90% for absorbers, where the frequency ranges are believed as effective absorption bandwidth (EAB) when the RL value is smaller than -10 dB [56, 57]. The EM wave absorption performance of $NiCo_2O_4$/C absorbers is presented in Fig. 4 and Fig. 5. For the NC360 absorber, the wide EAB of 9.6 GHz is achieved at 3.0 mm, and RL_{min} value reaches -66.15 dB at 1.5 mm (Fig 4a, i and m). For the NC380 absorber, the EAB reaches 8.96 GHz at 2.0 mm, and the RL_{min} value reaches as high as -75.26 dB at 1.5 mm (Fig 4b, j and n). The widest EAB of 9.92 GHz is obtained for the NC400 absorber at 4.5 mm, and RL_{min} value reaches -76.07 dB at 2.5 mm (Fig 4c, k and o). The excellent absorption performance, including a minimum reflection loss of -81.04 dB and a broad EAB of 7.92 GHz, is acquired for the NC420 absorber at a matched thickness of 3.5mm (Fig 4d, l, p). A numerical comparison of the EAB for the four types of absorbers with a matched thickness ranging from 1.5 to 4.5 mm can be visualized in Fig. 4i-l. In addition to paying attention to the EAB simply, the matching thickness factor should be strengthened, where the

NC360 absorber achieves a wider absorption band at a smaller matched thickness, i.e., 8.56 GHz at a matched thickness of 1.5 mm. Certainly, the EAB is more than 9.6 GHz at 3.0 mm; however, the smaller matched thickness makes it more valuable for applications. The results illustrate excellent absorption performance isobtained for each $NiCo_2O_4$/C absorber based on the reflection loss and EAB values.

For exploring deeper into the mechanism for achieving outstanding EM wave absorption properties of $NiCo_2O_4$/C absorbers, the impedance matching characteristic ($Z= |Z_{in}/Z_0|$) of the absorbers is displayed in Fig. 4e-h and Fig 5i-l. The value of $|Z_{in}/Z_0|$ close to 1.0 means the well match of the input impedance of the absorbers and impedance of the free space [58], where the incident EM wave can be permeated into absorbers as much as possible with less reflection. The results in Fig. 4e-h illustrate the impedance matching of the prepared $NiCo_2O_4$/C absorbers floating around 1.0 at a suitable matching thickness, except for the NC360. Especially, the impedance matching of NC380 absorber is 1.0 for each thickness at the minimum reflection loss, showing its superb impedance match. Besides, the impedance matching characteristic is evaluated by the delta-function method based on the Eqns. 12-14 [59, 60].

$$|\Delta| = |\sin h^2(Kfd) - M| \tag{12}$$

$$\mathrm{K} = \frac{\sin\left(\frac{\delta_e+\delta_m}{2}\right)\times 4\pi\sqrt{\mu'\varepsilon'}}{C\times\cos\delta_e\times\cos\delta_m} \tag{13}$$

$$\mathrm{M} = \frac{4\mu'\cos\delta_\mathrm{e}\times\varepsilon'\cos\delta_\mathrm{m}}{(\mu'\cos\delta_\mathrm{e}-\varepsilon'\cos\delta_\mathrm{m})^2+\left|\tan\left(\frac{\delta_\mathrm{m}-\delta_\mathrm{e}}{2}\right)^2\right|\times(\mu'\cos\delta_\mathrm{e}+\varepsilon'\cos\delta_\mathrm{m})^2} \tag{14}$$

where δ_e and δ_m are tangents of dielectric loss and magnetic loss, respectively. A value of $|\Delta|$ less than 0.4 means the well-matched input impedance of the absorbers and impedance of the free space, meaning the EM waves enter the absorber to a greater extent. Fig. 5i-l reveals the

two-dimensional (2D) color maps of |Δ| for the NC360, NC380, NC400 and NC420 absorbers at different thicknesses during 2-18 GHz, where the blue region means the value of |Δ| less than 0.4. The results obtained by comparing 2D images of the $NiCo_2O_4$/C absorbers imply the NC380 absorber owns the most prominent best impedance matching performance due to its largest blue area, while the NC360 has the smallest blue area. NC400 and NC420 absorbers also present large blue area, but other color areas gradually appear (|Δ|> 0.4) as the thickness decreases and the frequency increases, which indicate poor wave absorption performance at small matched thicknesses, agreeing with the analysis results in Fig. 4 e-h.

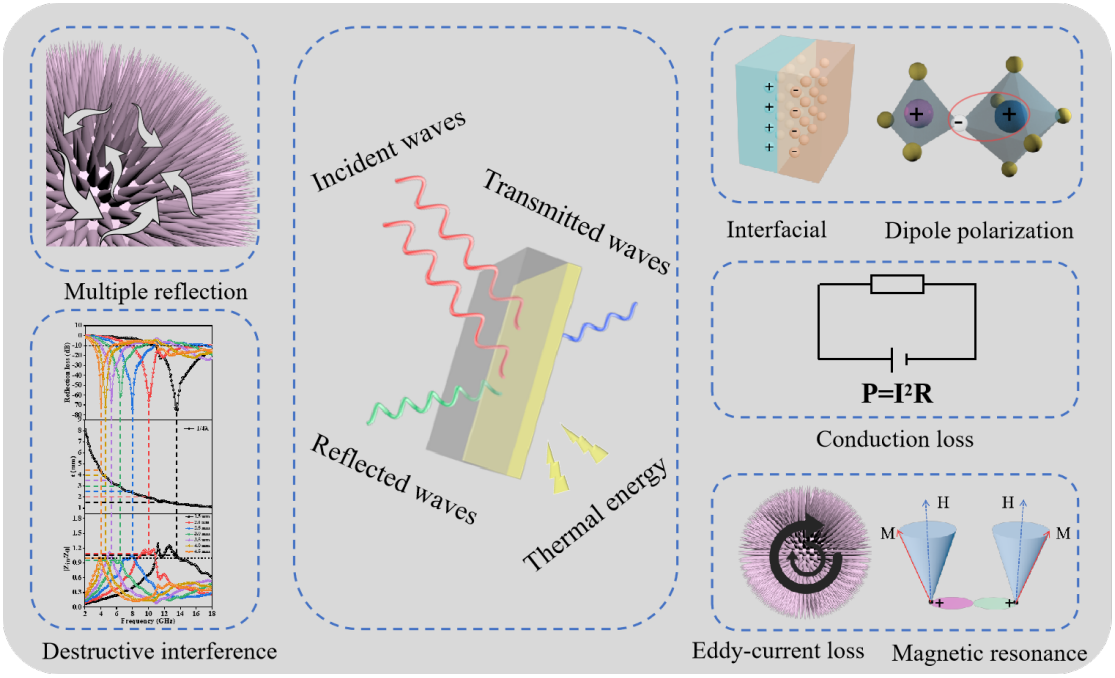

Fig. 6 EM waves absorption mechanism of the synthesized $NiCo_2O_4$/C absorbers

Fig. 6 further illustrates the EM wave absorption mechanism of urchin-shaped $NiCo_2O_4$/C absorbers. Well impedance matching characteristics allow EM waves to enter the absorber to the maximum extent and are exhausted under the cooperative effect of multiple loss mechanisms [60-62]. First, the EM waves entering the absorber are reflected and scattered multiple times

among the dense needle-like structures on the urchin-like surface and hollow structure [63，64]. The matching thickness, peak reflection loss and frequency of the prepared $NiCo_2O_4$/C absorbers satisfy the Quarter Wavelength Theory, which illustrates the reflected EM waves on the absorber surface and the incident EM waves are dissipated at 180° to each other, enhancing the attenuation of EM waves [28, 65]. Second, multiple heterogeneous interfaces are built in the $NiCo_2O_4$/C absorbers, especially between $NiCo_2O_4$ and carbon, lead to charge redistribution and subsequent interfacial polarization to enhance dielectric losses due to the different components have different abilities to retain charge [66-68]. Third, abundant oxygen vacancies are introduced into $NiCo_2O_4$/C absorbers, which trap carriers generated under alternating electric fields, leading to carrier accumulation, which can act as dipoles causing dipole polarization [69-71]. Besides, the high electrical conductivity of the carbon and $NiCo_2O_4$ allows electron transfer while forming microcurrents, and the dense needle-like structure increases the electron transfer pathway, improving the conductive loss capacity [72,73]. Finally, the inherent magnetic properties of nickel cobaltate can provide some magnetic loss capability, including eddy current loss and natural resonance [74]. **Table S2** shows a comparison of the EMW absorption performance of the previous works on $NiCo_2O_4$-based absorbers, which further proved the excellent performance obtained in this work.

3. Conclusions

In summary, the urchin-shaped $NiCo_2O_4$/C composites with hollow sphere structures are successfully prepared by facile hydrothermal and calcination processes. The impedance matching

characteristics are ameliorated by the unique urchin-shaped hollow morphology and the cooperative effect of multicomponent. Furthermore, the heterogeneous interfaces formed between the different components and the oxygen vacancy defects built during the calcination process are conducive to the enhancement of the polarization loss, thus enhancing the attenuation of EM waves. The results of the EM waves absorption performance tests show that the RL_{min} of the NC380 absorber reaches -75.26 dB at 1.5 mm and the EAB reaches 8.96 GHz at 2 mm, exhibiting the superb EM waves absorption properties and gigantic potential in practical application. This methodology of designing the unique urchin-shaped hollow structures and introducing heterogeneous interfaces and oxygen vacancy defects shed light on exploring bimetallic oxide-based or other oxides EM wave absorbers with satisfactory absorption properties.

Declaration of no interest

The authors declare that they have no known competing financial interests or personal relationships that could have appeared to influence the work reported in this paper.

Acknowledgments

This work was supported by National Natural Science Foundation of China (52207249), Natural Science Foundation of Shandong Province (ZR2022ME089), the research program of Top Talent Project of Yantai University (1115/2220001), Yantai Basic Research Project (2022JCYJ04) and the Science Fund of Shandong Laboratory of Advanced Materials and Green Manufacturing (AMGM2021F11). The authors would like to thank the Deanship of Scientific Research at Umm Al-Qura University for supporting this work by Grant Code: (22UQU4320141DSR72).

References

1. H.Y. Wang, P.P. Jin, J. Mater. Sci.: Mater. Electron. 29 (2018) 14643-14650.
2. F. Yan, J.Y. Kang, S. Zhang, C.Y. Li, C.L. Zhu, X.T. Zhang, Y.J. Chen, Nanoscale. 10 (2018) 18742-18748.
3. X.F. Zhou, Z.R. Jia, A.L. Feng, S.L. Qu, X.A Wang, X.H. Liu, B.B. Wang, G.L. Wu, J. Colloid Interface Sci. 575 (2020) 130-139.
4. M.L. Ma, W.T. Li, Z.Y. Tong, Y. Ma, Y.X. Bi, Z.J. Liao, J. Zhou, G.L. Wu, M.X. Li, J.W. Yue, X.Y. Song, X.Y. Zhang, J. Colloid Interface Sci. 578 (2020) 58-68.
5. Y.L. Zhang, J. Kong, J.W. Gu, Sci. Bull. 67 (2022) 1413–1415.
6. Y.L. Zhang, J. Kong, J.W. Gu, Sci. Bull. 67 (2022) 1413-1415.
7. Y.X. Han, M.K. He, J.W. Hu, P.B. Liu, Z.W. Liu, Z.L. Ma, W.B. Ju, J.W. Gu, Nano Res. 2022.
8. W.W. Wang, L.T. Yi, Y.Z. Zheng, J. Lu, A.S. Jiang, D. Wang, Composites Communications. 37 (2023) 101455.
9. C.B. Liang, J. He, Y.L. Zhang, W. Zhang, C.L. Liu, X.T. Ma, Y.Q. Liu, J.W. Gu, Compos. Sci. Technol. 224 (2022) 109445.
10. C.B. Liang, Z.J. Gu, Y.L. Zhang, Z.L. Ma, H. Qiu, J.W. Gu, Nano-Micro Lett. 13 (2021) 181.
11. L. Wang, Z.L. Ma, H. Qiu, Y.L. Zhang, Z. Yu, J.W. Gu, Nano-Micro Lett. 14 (2022) 224.
12. J.Y. Cheng, H.B. Zhang, Y.F. Xiong, L.F. Gao, B. Wen, Hassan Raza, H. Wang, G.P. Zheng, D.Q. Zhang, H. Zhang, J. Materiomics. 7 (2021) 1233-1263.
13. M.R. Han, Y.F. Yang, W. Liu, Z.H. Zeng, J.R. Liu, Sci. China Mater. (2022).
14. Z.L. Ma, X.L. Xiang, L. Shao, Y.L. Zhang, J.W. Gu, Angew. Chem. Int. Ed. 61 (2022) e202200705.
15. K.P. Ruan, J.W. Gu, Macromol. 55 (2022) 4134-4145.
16. K.P. Ruan, Y.Q. Guo, J.W. Gu, Macromol. 54 (2021) 4934−4944
17. X.J. Liu, M. Gao, J.Y. Chen, S. Guo, W. Zhu, L.C. Bai, W.Z. Zhai, H.J. Du, H. Wu, C.Z. Yan, Y.S. Shi, J.W. Gu, Hang Jerry Qi, K. Zhou, Adv. Funct. Mater. 32 (2022) 2203323
18. X.F. Zhou, Z.R. Jia, A.L. Feng, X.X. Wang, J.J. Liu, M. Zhang, H.J. Cao, G.L. Wu, Carbon. 152 (2019) 827-836.
19. G.L. Wu, Y.H. Cheng, Z.H. Yang, Z.R. Jia, H.J. Wu, L.J. Yang, H.L. Li, P.Z. Guo, H.L. Lv, Chem. Eng. J. 333 (2018) 519-528.
20. Y. Liu, X.F. Zhou, Z.R. Jia, H.J. Wu, and G.L. Wu, Adv. Funct. Mater. 32 (2022) 2204499.
21. H.L. Lv, X.D. Zhou, G.L. Wu, Ufuoma I. Karaa, X.G. Wang, J. Mater. Chem. A. 9 (2021) 19710-19718.
22. H.L. Lv, Z.H. Yang, B. Liu, G.L. Wu, Z.C. Lou, B. Fei, R.B. Wu, Nat. Commun. 12 (2021) 834.

23. J.W. Wen, X.X. Li, G. Chen, Z.N. Wang, X.J. Zhou, H.J. Wu, J Colloid Interface Sci. 594 (2021) 424-434.
24. B. Du, M. Cai, X. Wang, J.J. Qian, C. He, A.Z. Shui, J. Adv. Ceram. 10 (2021) 832-842.
25. B.B. Fan, S.P. Lv, W.H. Guo, H.L. Wang, G. Shao, H.X. Lu, H.L. Xu, D.L. Chen, R. Zhang, J. Mater. Sci.: Mater. Electron. 30 (2019) 17358-17362.
26. G.Y. Qin, X.X. Huang, X. Yan, Y.F. He, Y.H. Liu, L. Xia, B. Zhong, J. Adv. Ceram. 11 (2021) 105-119.
27. M. Qin, L.M. Zhang, X.R. Zhao, H.J. Wu, Adv Sci. 8 (2021) 2004640.
28. M. Qin, L.M. Zhang, H.J. Wu, Appl. Surf. Sci. 515 (2020) 146132.
29. M. Qin, H.S. Liang, X.R. Zhao, H.J. Wu, J Colloid Interface Sci. 566 (2020) 347-356.
30. C.P. Li, Y.Q. Ge, X.H. Jiang, Z.M. Zhang, L.M. Yu, J. Mater. Sci.: Mater. Electron. 30 (2019) 3124-3136.
31. Q.H. Zhu, Z.L. Zhang, Y.Y. Lv, X.Q. Chen, Z. Wu, S. Wang, Y.H. Zou, CrystEngComm. 21 (2019) 4568-4577.
32. J.L. Fan, W.J. Xing, Y. Huang, J.X. Dai, Q. Liu, F. Hu, G.L. Xu, J. Alloys Compd. 821 (2020) 153491.
33. L. Chai, Y.Q. Wang, Z.R. Jia, Z.X. Liu, S.Y. Zhou, Q.C. He, H.Y. Du, G.L. Wu, Chem. Eng. J. 429 (2022) 132547.
34. Q. Chang, H.S. Liang, B. Shi, X.L. Li, Y.T. Zhang, L.M. Zhang, H.J. Wu, J Colloid Interface Sci. 588 (2021) 336-345.
35. X.D. Wu, M. Wei, S.H. Yu, J.Y. Huang, R. Sun, C.P. Wong, SN Appl. Sci. 1 (2019) 170.
36. W. Zhong, Q.R. Ma, W.W. Tang, Y.K. Wu, W. Gao, Q.J. Yang, J.G. Yang, M.W. Xu, Inorg. Chem. Front. 7 (2020) 1003-1011.
37. C.X. Hou, W.Y. Yang, Hideo Kimura, X.B. Xie, X.Y. Zhang, X.Q. Sun, Z.P. Yu, X.Y. Yang, Y.P. Zhang, B. Wang, B.B. Xu, Deepak Sridhar, Hassan Algadi, Z.H. Guo, W. Du, J. Mater. Sci. Technol. 142 (2023) 185-195.
38. C.X. Hou, W.Y. Yang, X.B. Xie, X.Q. Sun, J. Wang, Nithesh Naik, D. Pan, X.M. Mai, Z.H. Guo, F. Dang, W. Du, J. Colloid Interface Sci. 596 (2021) 396-407.
39. W.Y. Yang, D.N. Peng, Hideo Kimura, X.Y. Zhang, X.Q. Sun, Rami Adel Pashameah, Eman Alzahrani, B. Wang, Z.H. Guo, W. Du, C.X. Hou, Adv. Compos. Hybrid Mater. 5 (2022) 3146-3157.
40. X.J. Zhou, J.W. Wen, Z.N. Wang, X.H. Ma, H.J. Wu, J Colloid Interface Sci. 602 (2021) 834-845.
41. H.J. Wu, M. Qin, L.M. Zhang, Composites, Part B. 182 (2020) 107620.
42. Y. Wu, K.H. Tian, R.W. Shu, J.B. Zhu, Y. Liu, C. Zhang, Y.N. Huang, Z.H. Chen, J. Colloid Interface Sci. 616 (2022) 44-54.
43. W. Wang, H. Zhang, Y.Z. Zhao, J.N. Wang, H.T. Zhao, P.B. Li, J.N. Yun, Z.H. Deng, Z.Y. Zhang, J.X. Tian, J.F. Yan, W. Zhao, F.C. Zhang, Chem. Eng. J. 426 (2021) 131667.
44. S.S. Wang, H.H. Zhu, Q.Z. Jiao, X.G. Jiao, C.H. Feng, H.S. Li, D.X. Shi, Q. Wu, Y. Zhao, New J. Chem. 45 (2021) 20928-20936.
45. G. Chen, L.M. Zhang, X.M. Fan, H.J. Wu, J Colloid Interface Sci. 588 (2021) 813-825.

46. Y.Y. Dong, X.J. Zhu, F. Pan, L. Cai, H.J. Jiang, J. Cheng, Z. Shi, Z. Xiang, W. Lu, Carbon. 190 (2022) 68-79.
47. Q. Chang, H.S. Liang, B. Shi, H.J. Wu, J Colloid Interface Sci. 600 (2021) 49-57.
48. N. Zhang, P.Z. Chen, W.X. Chen, Y. Wang, Compos. Sci. Technol. 204 (2021) 108643.
49. M. Qin, L.M. Zhang, H.J. Wu, Adv Sci. 9 (2022) 2105553.
50. T.Q. Hou, Z.R. Jia, A.L. Feng, Z.H. Zhou, X.H. Liu, H.L. Lv, G.L. Wu, J. Mater. Sci. Technol. 68 (2021) 61-69.
51. H.S. Liang, H. Xing, Z.H. Ma, H.J. Wu, Carbon. 183 (2021) 138-149.
52. Z. Xu, Y.C. Du, D.W. Liu, Y.H. Wang, W.J. Ma, Y. Wang, P. Xu, X.J. Han, ACS Appl. Mater. Interfaces. 11 (2019) 4268-4277.
53. C.X. Hou, G.H. Fan, X.B. Xie, X.Y. Zhang, X.Q. Sun, Y.P. Zhang, B. Wang, W. Du, R.H. Fan, J. Alloys Compd. 855 (2021) 157499.
54. N.N. Wu, B.B. Zhao, J.Y. Liu, Y.L. Li, Y.B. Chen, L. Chen, M. Wang, Z.H. Guo, Adv. Compos. Hybrid Mater. 4 (2021) 707-715.
55. N.N. Wu, B.B. Zhao, X.Y. Chen, C.X. Hou, M.N. Huang, A. Alhadhrami, Gaber A. M. Mersal, Mohamed M. Ibrahim, J. Tian, Adv. Compos. Hybrid Mater. 5 (2022) 1548-1556.
56. K. Li, Y. Shen, L.H. Xu, H. Pan, N. Shen, H.L. Ling, K. Ni, Z.W. Ni, G.H. Xiang, Vacuum. 205 (2022) 111493.
57. K.H. Tian, Y. Wu, R.W. Shu, Y. Liu, Y.N. Huang, Z.H. Chen, G.J. Cheng, Mater. Lett. 295 (2021) 129825.
58. Y. Mu, L.M. Zhang, H. Liu, H.J. Wu, J. Mater. Sci.: Mater. Electron. 32 (2021) 26059-26073.
59. X.G. Su, J. Wang, X.X. Zhang, Z.J. Liu, W. Dai, W. Chen, B. Zhang, Ceram. Int. 46 (2020) 19293-19301.
60. X.B. Xie, B. Zhang, Q. Wang, X.H. Zhao, D. Wu, H.T. Wu, X.Q. Sun, C.X. Hou, X.Y. Yang, R.H. Yu, S.Z. Zhang, Vignesh Murugadoss, W. Du, J Colloid Interface Sci. 594 (2021) 290-303.
61. B. Du, D.Y. Zhang, J.J. Qian, M. Cai, C. He, P. Zhou, Adv. Compos. Hybrid Mater. 4 (2021) 1281-1291.
62. X.L. Cao, Z.R. Jia, D.Q. Hu, G.L. Wu, Adv. Compos. Hybrid Mater. 5 (2022) 1030-1043.
63. Y.F. Wang, P. Wang, Z.R. Du, C.T. Liu, C.Y. Shen, Y.M. Wang, Adv. Compos. Hybrid Mater. 5 (2021) 209-219.
64. M. Zhang, C. Han, W.Q. Cao, M.S. Cao, H. J. Yang, J. Yuan, Nanomicro Lett. 13 (2020) 27.
65. Y.L. Zhang, K.P. Ruan, J.W. Gu, Small. 17 (2021) 2101951.
66. X.M. Huang, X.H. Liu, Z.R. Jia, B.B. Wang, X.M. Wu, G.L. Wu, Adv. Compos. Hybrid Mater. 4 (2021) 1398-1412.
67. X.F. Zhang, L.L. Xu, J.T. Zhou, W.J. Zheng, H. Jiang, Karma Zuraiqi, Gang Kevin Li, J. Liu, Ali Zavabeti, ACS Appl. Nano Mater. 4 (2021) 9200-9212.
68. X.F. Zhou, Z.R. Jia, X.X. Zhang, B.B. Wang, X.H. Liu, B.H. Xu, L. Bi, G.L. Wu, Chem. Eng. J. 420 (2021) 129907.

69. L.B. Zhao, Y.Y. Guo, Y.X. Xie, T.T. Cheng, A.L. Meng, L.Y. Yuan, W.X. Zhao, C.L. Sun, Z.J. Li, M. Zhang, Appl. Surf. Sci. 592 (2022) 153324.
70. G.Y. Qin, X.X. Huang, X. Yan, Y.F. He, Y.H. Liu, L. Xia, B. Zhong, J. Adv. Ceram. 11(2021) 105-119.
71. X.J. Zeng, C. Zhao, Y.C. Yin, T.L. Nie, N.H. Xie, R.H. Yu, Galen D. Stucky, Carbon. 193 (2022) 26-34.
72. Y.Y. Dong, X.J. Zhu, F. Pan, L. Cai, H.J. Jiang, J. Cheng, Z. Shi, Z. Xiang, W. Lu, Carbon. 190 (2022) 68-79.
73. Y.Y. Dong, X.J. Zhu, F. Pan, B.W. Deng, Z.C. Liu, X. Zhang, C. Huang, Z. Xiang, W. Lu, Adv. Compos. Hybrid Mater. 4 (2021) 1002-1014.
74. X.K. Lu, D.M. Zhu, X. Li, M.H. Li, Q. Chen, Y.C. Qing, Adv. Compos. Hybrid Mater. 4 (2021) 946-956.